



Interfibrillar stiffening of echinoderm mutable collagenous tissue demonstrated at the nanoscale.

Mo, J; Prévost, SF; Blowes, LM; Egertová, M; Terrill, NJ; Wang, W; Elphick, MR; Gupta, HS

Freely available online through the PNAS open access option.

For additional information about this publication click this link.

<http://qmro.qmul.ac.uk/xmlui/handle/123456789/15948>

Information about this research object was correct at the time of download; we occasionally make corrections to records, please therefore check the published record when citing. For more information contact scholarlycommunications@qmul.ac.uk

Interfibrillar stiffening of echinoderm mutable collagenous tissue demonstrated at the nanoscale

Jingyi Mo¹, Sylvain Prévost², Liisa M. Blowes³, Michaela Egertová³, Nick J. Terrill⁴, Wen Wang^{1,5}, Maurice R. Elphick^{3,*}, and Himadri S. Gupta^{1,5*}

1. Queen Mary University of London, School of Engineering and Material Science, London, E1 4NS, UK

2. Beamline ID02, European Synchrotron Radiation Facility, Grenoble, France

3. Queen Mary University of London, School of Biological and Chemical Sciences, London, E1 4NS, UK

4. Diamond Light Source, Harwell Science and Innovation Campus, Harwell, UK

5. Institute of Bioengineering, Queen Mary University of London, London, E1 4NS, UK

Abstract

The mutable collagenous tissue (MCT) of echinoderms (e.g. sea cucumbers and starfish) is a remarkable example of a biological material that has the unique attribute, among collagenous tissues, of being able to rapidly change its stiffness and extensibility under neural control. However, the mechanisms of MCT have not been characterised at the nanoscale. Using synchrotron small-angle X-ray diffraction to probe time-dependent changes in fibrillar structure during *in situ* tensile testing of sea cucumber dermis, we investigate the ultrastructural mechanics of MCT by measuring fibril strain at different chemically-induced mechanical states. By measuring a variable interfibrillar stiffness (E_{IF}), the mechanism of mutability at the nanoscale can be demonstrated directly. A model of stiffness modulation *via* enhanced fibrillar recruitment is developed to explain the biophysical mechanisms of MCT. Understanding the mechanisms of MCT quantitatively may have applications in development of new types of mechanically tuneable biomaterials.

*Corresponding authors:

Dr. Himadri S. Gupta, School of Engineering and Materials Science, Queen Mary University of London, London, UK; email: h.gupta@qmul.ac.uk

Prof. Maurice R. Elphick, School of Biological and Chemical Sciences, Queen Mary University of London, London, UK; email: m.r.elphick@qmul.ac.uk

Significance statement:

Collagen plays crucial biomechanical roles in a wide array of animal tissues, but its mechanical properties remain largely static over short timescales. However, echinoderms (sea cucumbers, starfish) are striking exceptions to this rule, having “mutable collagenous tissue” with changeable mechanical properties, enabling complex locomotion, postural maintenance, defence and reproductive strategies. Using a high resolution X-ray probe which measures how the building blocks – fibrils – of echinoderm connective tissue stretch, slide or reorient in real time, we show that sea cucumbers achieve this remarkable property by changing the stiffness of the matrix between individual fibrils, rather than the properties of the fibrils themselves. Understanding the mechanisms of mutability in this unique tissue may help design novel mechanically tuneable synthetic biomaterials.

Introduction

The mechanical properties of biological tissues are usually optimized to operate within specific physiological loading and strain ranges (1, 2). With the exception of the common phenomenon of strain stiffening that occurs during mechanical loading (3), material-level changes in the overall mechanical properties of tissues typically occur slowly, driven by growth, remodelling or ageing (4). The molecular level mechanisms underpinning these changes often involve permanent, irreversible changes, including covalent crosslinking *via* disulphide bridges in tendon (5), formation of metal-ion/protein complexes (6), or replacement of water with an inorganic phase as in biomineralization (7), although viscoelastic mechanical responses may involve transient cross-linking (8). In contrast, changes in the mechanical properties of animal tissues that occur actively and reversibly within a few seconds are canonically mediated by ATP-dependent molecular motors, as in muscle (9). A notable exception is the mutable collagenous tissue (MCT) of echinoderms (e.g. starfish, sea urchins, sea cucumbers), which undergoes rapid changes in stiffness under the control of the nervous system via ATP-independent mechanisms (10-12). MCT is ubiquitous in echinoderms (12); for example in the dermis (skin) of sea cucumbers (13, 14), the compass depressor ligament (CDL) of sea-urchins (15-17), and in the arms of feather stars (18). The presence of MCT enables functionally diverse behaviours; for example in

starfish, MCT enables body wall stiffening during feeding on prey and it also enables irreversible body wall softening prior to arm autotomy as a defence against predation (12). Thus, MCT represents an evolutionary adaptation of collagenous tissue to change mechanical properties dynamically, whilst in other phyla collagenous tissues largely act as passive mechanical springs. The benefits of MCT also include a much lower energy expenditure (19) compared with muscle tissue and the presence of MCT is considered to have been a major factor in the evolutionary success and ecological diversity of echinoderms (reviewed in Barbaglio et al (20)).

The initial identification of connective tissue of echinoderms as having mechanically unusual properties – illustrated by its denotation as “catch” connective tissue – was through the observed stiffening and softening response of such tissues to sea water of different ionic compositions, as well as neurotransmitters (e.g. acetylcholine) (14) and drugs (e.g. cocaine) (21). Such chemical means to induce mutability in MCT remain a convenient and reproducible method to induce mechanically altered states (15, 22, 23). Specifically, previous studies demonstrated that alteration of extracellular Ca^{2+} and K^{+} levels modulates the stiffness of living tissues in sea urchin spine ligaments (14, 24-28), holothurian dermis (13, 22, 29, 30) and starfish (30). Increased K^{+} concentration increases the stiffness of these particular examples of MCT, while decreased Ca^{2+} concentration lowers stiffness, when compared to artificial sea water (ASW) as a reference solution. The changes induced by these chemical methods are within the same order of magnitude as physiologically relevant mechanical changes occurring in MCT *in vivo*: under mechanical stimulation (pressing the tissue by hand), starfish body wall MCT stiffens by a factor of ~3.3 (30), while increasing K^{+} concentration leads to an increase of ~6.1 (30). Conversely, the reduction of stiffness in calcium free artificial sea water is considerable (31), which is comparable to the reduction to zero in the extreme case of limb autotomy where the tissue disintegrates structurally (32).

The unusual mechanical properties of MCT must arise from the micro- and ultrastructure of this tissue, which shows both commonalities with, as well as some clear differences from, the more familiar vertebrate collagenous tissues such as skin, tendon and bone. At the molecular level, the collagen of sea cucumber MCT is different from heterotrimeric vertebrate type I fibrillar collagen, consisting of homotrimers with three α_1 polypeptide chains (12). These collagen molecules aggregate into discontinuous spindle-shaped collagen fibrils with a mean

diameter of ~17 nm (33). Proteoglycans are bound to the fibrillar surfaces, which along with non-collagenous proteins such as tensilin, stiparin, softenin and fibrosurfin comprise the interfibrillar matrix (34-36). Together with fibrillin-rich microfibrils (34) the fibrillar collagen network comprises the bulk of the extracellular matrix (ECM) of MCT. Dispersed in this ECM are clusters of juxtaligamental cells (JLCs) (12, 19, 24, 28, 29) (15) (as seen from transmission-electron and light microscopy), which are MCT-effector cells that are under neural control (12, 15). Furthermore, it is the innervation of MCT that is a key distinction between echinoderm and vertebrate collagenous tissues (15).

Initial hypotheses about the ultrastructural mechanism enabling the mechanical mutability described above focused on ion-mediated creation of physical crosslinks between fibrils and within the interfibrillar matrix in the ECM(11, 37). Divalent calcium ions were proposed to be especially effective in increasing interfibrillar matrix stiffness, and their depletion in Ca^{2+} -free sea water solutions was believed to be a major reason for the reduced stiffness. However, this hypothesis was disproved when cell-lysed MCT showed no mechanical mutability in the presence of such solutions (38). It is therefore believed that the ionic treatments directly affect cellular secretion pathways in the JLCs, inducing release of proteins that alter interfibrillar binding, thus changing the stiffness of the tissue(12). Several such proteins, including tensilin, softenin and novel stiffening factor (NSF) have been identified (31, 34, 35, 39, 40). It is believed that the JLCs secrete such effector proteins as a result of external stimuli (such as touch, aggressive attack, or alteration in the ionic strength of the sea water around the animal), thereby changing the stiffness of the tissue. Biochemical evidence to support this hypothesis includes the structural similarity of some of these proteins to the tissue inhibitors of matrix metalloproteinases (TIMPs) found in vertebrates (41). Consistent with this notion, it has also been suggested that cysteine-rich sea urchin fibrillar domains (SURFs), found so far in the sea urchin collagen 2 α and 5 α N-propeptides, as well as fibrosurfin (an interfibrillar protein) (36, 42), play a role in enabling mutability. The 2 α N-propeptides and fibrosurfin co-localise on collagen fibril surfaces in adult sea urchins. However, despite this considerable level of biochemical insight into MCT (12), the biophysical mechanisms by which the alteration in mechanics is mediated by the nanostructure – whether at the fibrillar or intrafibrillar level – are still not completely understood.

Techniques used to correlate ultrastructure with mechanics have been by necessity largely static and indirect, including imaging tissue after alteration of mechanical state with techniques like transmission electron microscopy (15). These introduce unavoidable artefacts from sample preparation and do not measure the changes as they occur in real-time. The use of *in situ* synchrotron X-ray diffraction to provide molecular- and supramolecular level images of the ultrastructural conformation during alteration of the mechanical state of MCT is a direct way to overcome these limitations (43-46). The axial periodicity of electron density along the long axis of collagen fibrils (47), with a repeat distance of $D \sim 65\text{-}67\text{ nm}$, leads to Bragg diffraction peaks in X-ray scattering in the small-wavevector domain ($< 5\text{ nm}^{-1}$) characteristic of small angle X-ray diffraction (SAXD) (47). Shifts in these peaks, as would be induced by mechanical loading or ionic treatments, are therefore a measure of the nanoscale fibril strain as demonstrated for vertebrate tissues (43-45, 48, 49). By combining micromechanics with *in situ* small-angle X-ray scattering, it has been possible to shed light on the fundamental ultrastructural mechanisms enabling viscoelasticity, toughness and force generation in vertebrate tissues ranging from tendon(50), bone (46, 48), aorta (51) to muscle (52), as well as more unusual examples of biological optimization such as armoured fish scales (45). Using SAXD, it was found that in cross-link deficient fibrils, increased molecular slippage led to larger fibril strains, compared to normal collagen fibrils (50), that high toughness of antler bone was due to inorganic/organic friction at the intrafibrillar level (43), and that fibrillar reorientation blunted crack propagation in skin (53), among other examples.

When combined with high-intensity synchrotron X-ray sources, time-resolved SAXD with *in situ* micromechanical loading could be employed to quantify the fibrillar deformation mechanisms of MCT in various states of mechanical mutability, thus clarifying the biophysical mechanisms enabling this remarkable behaviour. Here, we apply these techniques to the sea cucumber dermis as a model system (Fig. 1). Understanding the molecular mechanisms enabling mutability may have applications in developing dynamic biomaterials, systems capable of changing their mechanical properties and the design of mechanically tuneable implants. The adaptive mechanical properties in MCT could, for example, provide insight into the repair of connective tissue pathologies in soft tissue, such as therapy in tendon or ligament weakening resulting from surgery or immobilisation (12), the design of implants capable of generating active forces, and in the area of neural implants where variable stiffness during insertion and implantation have been proposed (54).

Results

Synchrotron SAXD measurements of fibrillar strain in MCT from sea cucumber dermal tissue were carried out at beamline ID02 at the European Synchrotron Radiation Facility (Grenoble, France) as shown in Fig. 2. Prior to testing, tissue specimens were chemically incubated in artificial sea water (ASW) and two ionically modified solutions of ASW (potassium rich ASW (KASW) and calcium free ASW (CaF-ASW)) which are known to induce standard state, stiffening and softening of sea cucumber dermis respectively (22, 37) (for details see *Materials and Methods*). The fibril strain ϵ_F is the fractional increase in fibril length (as measured from the shifts in the meridional Bragg peaks in the SAXD pattern of MCT collagen fibrils), while tissue strain ϵ_T is the fractional increase in MCT sample length and tissue stress σ_T is the force divided by sample area (See *Materials and Methods*). Considering the fibrillar-level strain ϵ_F and tissue stress developed in MCT during stretch to failure tests, it is observed (Fig. 3(a)) that fibrils in tissues with different chemical stimulation - CaF-ASW, ASW and KASW - show a differing extent of elongation at the same tissue strain ϵ_T . At a given tissue strain, the amount of fibril strain is proportional to the stress taken up by the fibrils. At a tissue strain ϵ_T around 10%, fibrils in KASW-tissue have a much higher extension of ~0.5% compared to ASW (0.07%). Likewise, the fibril strain for CaF-ASW is much lower (~0.001%), indicating mainly interfibrillar sliding. The maximum fibril strain developed in KASW is much larger than in CaF-ASW, and the fibril strain in ASW is in between that of KASW and CaF-ASW. Fig. 3(b) shows corresponding averaged mean strain-stress curves for body wall tissue in KASW (red), ASW (black) and CaF-ASW (blue). The averaged macroscopic stress σ_T with tissue strain ϵ_T at 40% for KASW-treated (4.08 MPa) specimens is significantly higher than CaF-ASW (0.13 MPa), while the ASW-treated (0.77 MPa) specimens are in between these extremes. We note that the increase of fibril strain with applied tissue strain is not completely smooth in all cases, as evidenced by the error bars. This is most noticeable in the case of KASW-treated tissue, where there are clear local peaks at ~10 and 30% strain followed by dips. The structural reasons for this behaviour will be considered further when the model to explain fibrillar deformation is developed in the Discussion. Further, the variation of the macroscopic tensile stress (at the tissue-level) for the whole specimen for all treatments (KASW, ASW and CaF-ASW) is much greater compared to the strain developed at the fibril-level (Fig. 3a), indicating that interfibrillar components of the extracellular matrix are important in mechanisms of MCT.

The differences in Ca^{2+} or K^{+} concentrations in CaF-ASW, ASW and KASW led to changes of maximum tangent modulus and maximum tissue stress (Fig. 4). Ca-FASW-treated (0.69±0.59 MPa) samples had ~80% lower maximum tangent modulus compared to ASW (3.23±0.40 MPa), while the maximum tangent modulus for KASW-treated samples (17.27 ±6.70 MPa) was 4 times larger. Concurrently, the maximum stress of each state is very different, with the loads borne by CaF-ASW-treated tissue (0.30 ± 0.32 MPa) being much less (~80 %) compared to ASW-tissue (1.30 ± 0.20 MPa) while KASW-tissue (6.39 ± 0.44 MPa) had maximum stress 4 times higher than the control. Similarly, nanoscale parameters like fibril strain also show clear differences between treatments (Fig. 4(c) and (d)). Compared to maximum fibril extension (Fig. 4(c)) developed in KASW (0.94%), fibrils in CaF-ASW (0.09%) and ASW (0.35%) had a reduced elongation, with ~95% and 80% less strain respectively. Fig. 4(d) shows the ratio of fibril strain to tissue strain (ϵ_F/ϵ_T) for the three states, which is observed to be consistent with Fig. 4(c), showing that stiffened tissue sections have (ϵ_F/ϵ_T) of 0.044, larger than control specimens, whilst softened tissue sections have almost negligible fibril strain take-up ($\epsilon_F/\epsilon_T \sim 0$). The parameter ϵ_F/ϵ_T will be used to confirm the modelling results, which will be illustrated later.

In a complementary manner, we consider the alterations in the fibril orientation distribution on application of external load. The ν -parameter, derived from the angular distribution of the SAXD intensity, is a dimensionless number which is zero when fibrils are distributed at all angles with equal likelihood, and positive when fibrils are aligned either along one or a couple of principal directions (See *Materials and Methods*). A representative plot of the ν -parameter as a function of tissue strain (Fig. 5(a)) exhibits an initially high value of ~1.3 (corresponding to two main fibril directions equidistant (azimuthally) from the vertical direction) that is followed by a decrease to a minimum around 20% tissue strain. The initial two directions correspond to two principal helical fibre pitches along the long axis of the animal. The initial reduction in the ν -parameter corresponds to a more random fibril orientation, as indicated schematically in Fig. 5 (a-c), and represents the stress-induced breakdown of the two main fibril directions into a single broad distribution centred on the (vertical) direction of applied tensile load. For tissue strains larger than 20%, the ν -parameter increases monotonically with increasing tissue strain, before levelling off near tissue strains of ~40-50% close to macroscopic failure. The increase of the ν -parameter represents a narrowing of the azimuthal width of the initial broad fibril distribution around the direction of

Link to PNAS website (open access): <http://www.pnas.org/cgi/doi/10.1073/pnas.1609341113>

applied load. The tissue strain at the transition between the reduction of the ν -parameter and the subsequent increase is denoted by ε_{Tr} . The analysis of mean ε_{Tr} across three groups of specimens is shown in Fig. 5(d). The results indicate that soft (CaF-ASW) samples always have a higher ε_{Tr} , relative to the control (ASW) and stiffened (KASW) samples, which implies that the rate of reorientation (from the initial distribution with two main directions to a random and then highly oriented distribution) is slower for the softened MCT.

Model and Discussion

These experimental results, showing clear alterations in the deformation at the fibrillar level when MCT is stimulated into its stiff and soft states, can be used to build a simple model that sheds light on the key biophysical mechanisms enabling mutability (31, 34, 35, 39, 40). Prior research has proposed, but not directly demonstrated, that certain proteins secreted by JLCs including tensilin (38, 39), stiparin (34) and NSF (31) act to cross-link the fibrils. A complete ultrastructural mechanism for MCT mutability has not, however, been quantitatively established, and each protein appears to only be involved in a specific subset of the mechanical response, such as in stiffening a compliant specimen back to the reference state (as is the case for tensilin (38, 39)). At the ultrastructural level, the parallel-packed fibrils and interfibrillar matrix of MCT can be represented as shown in Fig. 6(a). The covalently cross-linked $(\alpha 1)_3$ collagen fibrils are expected to have much greater stiffness (~ 0.5 -2 GPa(55)) than the interfibrillar matrix (which can be considered a negatively charged hydrated gel (56)), although precise values for the interfibrillar matrix modulus are unknown. Under tensile loading, the highly anisotropic fibrillar structure together with the expected stiffness mismatch between the fibrils and the interfibrillar matrix will lead to a characteristic inhomogeneous deformation field at the nanoscale. In this deformation field, tensile forces develop in the fibrils and matrix, and significant shear occurs in the interfibrillar matrix connecting fibrils (57). The shearing force lines are shown in the insets in Fig. 6(b), and can be considered as representations of the cross-linking between fibrils proposed previously (12). Consequently, the fibril strain is only a fraction of the total strain (due to the remaining shearing strain in the interfibrillar matrix).

In order to keep the model analytically simple we consider a unidirectional fibre composite; whilst the initial unstrained MCT shows two main fibril directions around the direction of stretch (Fig. 5(b)), it is observed that for tissue strains larger than $\sim 20\%$ the fibrils are highly

aligned to the direction of applied stress and the uniaxial fibril arrangement is expected to be a good approximation for this region at least. This type of model, denoted a staggered model, has been proposed before, by us (43) and others (57, 58) for deformation of the ultrastructure of bone mineralized fibrils, tendon, enamel and dentine (48, 59), where a similar high stiffness element in tension (e.g. mineral platelet) is effectively in serial-loading with a low stiffness element loaded in shear (e.g. collagen fibrils). The deformation of the fibril ε_F , shear of the interfibrillar matrix γ_{IF} , and tissue level stress σ_T , among other quantities, have been calculated from load-balance equations at the nanoscale (43). These lead to expressions for the fibril to tissue strain ratio, and the tissue modulus E_T , in terms of the structural and constitutive parameters:

$$\frac{\varepsilon_T}{\varepsilon_F} = 1 + \frac{4}{\rho_1^2} \frac{1 - \Phi_1}{\Phi_1} \frac{E_F}{\gamma_{IF} E_{IF}} \quad \text{Equation 1}$$

$$E_T = \Phi_1 E_F \frac{\varepsilon_F}{\varepsilon_T} + (1 - \Phi_1) E_{IF} = \frac{\Phi_1 E_F}{1 + \frac{4}{\rho_1^2} \frac{1 - \Phi_1}{\Phi_1} \frac{E_F}{\gamma_{IF} E_{IF}}} + (1 - \Phi_1) E_{IF} \quad \text{Equation 2}$$

In the equations above, Φ_1 denotes the fibril volume fraction, ρ_1 the fibril aspect ratio, E_F the fibril elastic modulus, E_{IF} the interfibrillar modulus, and $\gamma_{IF} \sim 0.40$ is the ratio between shear (G_{IF}) and tensile (E_{IF}) modulus of the interfibrillar matrix ($G_{IF} = \gamma_{IF} E_{IF}$) (43); other terms have been defined earlier in the text. As our scheme enables measurement of deformation at the fibrillar level concurrently with tissue-level mechanical stress and strain, a parametric variation of fibril strain and tissue modulus may now be carried out and compared to the experimental results reported earlier in Fig. 4 and 5. These results are shown in Fig. 6(b) and discussed below.

Considering, for the moment, that the collagen fibrils have a constant elastic modulus E_F , we first examine the effects of altering the interfibrillar modulus on the change in tissue stiffness. Such a scenario corresponds to an alteration in cohesion due to secretion of stiffening factors such as tensilin, stiparin and NSF. As seen in **Equation 2**, the increase in tissue stiffness arises due to both the increased load borne by the interfibrillar matrix (second term on the right hand side in **Equation 2**) as well as – much more significantly – the increased stress borne by the collagen fibril due to the larger shear stress transferred by the interfibrillar matrix (first term on the right hand side). The stress borne by the collagen fibril is large due to the large contact surface area between the fibrils and the interfibrillar matrix due, in turn,

to the large fibril aspect ratio ρ_1 . Concurrently with the increase in tissue stiffness, the fibril strain increases as a fraction of the tissue strain, as larger tensile forces are transferred to the elastic fibrils with increased fibril strain.

In order to compare the model predictions with experimental data (Fig. 6(b) and (c)), initial estimates of some of the unknown parameters need to be made. The length and fibril diameter distributions for echinoderm collagen fibrils have been estimated previously (33, 60). While the maximum and minimum values span a wide range, a constant spindle shaped morphology was reported (33). The most frequent value (mode) in the diameter distribution was ~ 100 nm (60), and the length ranged from $50 \mu\text{m}$ to 1 mm. Using the constant shape of the collagen fibrils reported previously (33) and the diameter distribution shown in (60), these values can be used to estimate the maximal length to be $\sim 120 \mu\text{m}$. These lead to an aspect ratio of ~ 1000 . The fibril modulus for individual sea cucumber fibrils isolated from the tissue was measured to be ~ 500 MPa (55). As described in the *Supplementary Information*, these values can be used, together with the experimentally determined values of ϵ_F/ϵ_T and E_T , to obtain estimates of fibril volume fraction $\Phi_1 \sim 0.54$ and the interfibrillar modulus $E_{IF} \sim 50 \times 10^{-6}$ MPa (in the ASW-case). The fibril volume fraction will not vary across treatments, but the interfibrillar modulus will change. With these numerical values, the two trends described above – increase in both tissue stiffness (E_T) as well as in fibril strain ratio ϵ_F/ϵ_T with increasing E_{IF} – are plotted in Fig. 6(b), together with the experimentally measured values for the softened, control and stiffened groups. **Equation 1** is used to calculate interfibrillar matrix stiffness E_{IF} for each tissue group from measured ϵ_F/ϵ_T , which are then plotted (symbols) together with model curves (lines). In a similar manner, **Equation 2** is used to obtain E_{IF} from measured tissue moduli E_T for each group. For consistency of the model, the two calculated sets of E_{IF} should match, and indeed, it is observed that both methods give similar values for E_{IF} across the tissue groups.

In principle, however, there are two distinct ways in which the stiffness of MCT can be modified: either by the interfibrillar matrix stiffening (as considered above) or by alterations of the mechanics of the collagen fibrils, possibly by modulation of intrafibrillar cohesion. These two scenarios – fibrillar versus interfibrillar stiffening – lead to different behaviours at the fibrillar level. In the fibrillar stiffening case, the fibrillar strain (as a fraction of tissue strain) will reduce as the tissue stiffens, whilst in the interfibrillar stiffening case, the fibrillar

strain will increase as the tissue stiffens, as can be seen by combining **Equations 1** and **2** to obtain parametric plots of $\varepsilon_F/\varepsilon_T$ and E_T as functions of E_{IF} and E_F .

$$\frac{\varepsilon_F}{\varepsilon_T} = \frac{E_T - (1 - \Phi_1)E_{IF}}{\Phi_1 E_F} \quad \text{Equation 3}$$

In the model, changing the aspect ratio by $\pm 10\%$ leads to a variation of 20 % in both $\varepsilon_F / \varepsilon_T$ and E_T (*Supplementary Information*, section 2). In order to conclusively demonstrate interfibrillar stiffening, and exclude fibrillar stiffening as the key mechanism for mechanical changes in MCT, the experimental data for $\varepsilon_F/\varepsilon_T$ and E_T are plotted in Fig. 6(c) together with two sets of three predictive curves from the model. The first set of three curves (solid lines) corresponds to a continuous increase in interfibrillar modulus (for several discrete values of fibrillar stiffness), while the second set (dashed lines) corresponds to continuously increasing fibrillar stiffness for several values of interfibrillar stiffness. It is clearly seen that the experimental data show an increase in $\varepsilon_F/\varepsilon_T$ with E_T , corresponding to the case of interfibrillar matrix stiffening. Further, it is apparent that the mean values lie along the predicted curve for a collagen fibril modulus $E_F = 600$ MPa, which is close to the value of 500 MPa reported by Eppell et al (55). This finding provides evidence in support of the long-held, but not directly demonstrated, hypothesis that the alteration of MCT mechanical properties arises due to changes in interactions between fibrils (through changes in the interfibrillar matrix) rather than alterations in the mechanical properties of the fibrils themselves (12).

From the variation of interfibrillar matrix stiffness certain observations can be made. In MCT, E_{IF} is, even in the stiffest state, ~ 0.25 kPa - at least 6 orders of magnitude lower than the stiffness of the fibril ~ 0.6 GPa. In the state of least stiffness, there is a factor of ~ 100 reduction in E_{IF} relative to the already low value of 0.25 kPa, to ~ 5 -10 Pa, and the matrix can be considered a fluid. However, the increased stiffness of MCT in the stiffened state (necessary for its physiological maintenance of posture or locomotion (12)) is almost entirely due to the increased fibrillar recruitment to bear stress, and not due to the stress carried in the interfibrillar matrix. The ratio of the stress in the interfibrillar matrix to that in the fibril can be calculated from:

$$\frac{\sigma_{IF}}{\sigma_F} \approx \left(\frac{1 - \Phi_1}{\Phi_1} \right) \left(\frac{E_{IF}}{E_F} \right) \left(\frac{\varepsilon_T}{\varepsilon_F} \right) = \left(\frac{0.46}{0.54} \right) \left(\frac{50 \times 10^{-6}}{0.6} \right) \left(\frac{1}{0.01} \right) = 7.1 \times 10^{-3}$$

i.e. only ~0.7% of the total stress is borne by the interfibrillar matrix. Under alteration of mechanical state, the relative increase in fibril stress can be calculated from the change in fibril strain ratio, *via*

$$\sigma_F = \Phi_1 E_F \frac{\theta_F}{\theta_T}$$

We observe that fibril stress increases by a factor of ~4 (Fig. 4(d)) in the stiff state compared to the standard state. Conversely, in the softened state, the fibril stress decreased by a factor of ~10 relative to the standard state. We also note that we have (for simplicity) considered the interfibrillar matrix to stiffen homogeneously. In practice, there can be local heterogeneities (both temporal and spatial) in stiffness, possibly due to conformational changes in the non-collagenous proteins, local entanglements and other phenomena. Such heterogeneities would lead to local increases (or decreases) in interfibrillar stiffness, which would increase (or decrease) stress transfer between fibrils. Such alterations in stress transfer would explain the local maxima and minima in the fibril strain measured in stiffened KASW-treated MCT observed in Fig. 3(a). In this regard, the recent finding of collagen molecular shortening – due to water content changes – leading to large tensile stresses in tendon may be of relevance (61).

These findings shed light on the synergistic action at the nanoscale enabling mutability in MCT. By itself, the stress in the stiffened (or softened) interfibrillar matrix is by no means sufficient to account for the change in tissue stiffness. However, due to the large anisotropy and surface to volume ratio of the fibrils, considerable contact area exists for binding of the interfibrillar proteins and glycosaminoglycans to the fibrils. Such binding is likely to occur at the gap-zones (separated by $D \sim 65\text{-}67$ nm) identified previously as putative binding sites for proteoglycans in collagens (62). As a result, the total stress transferred to the collagen fibrils is effectively amplified by the anisotropy factor $\rho \sim 1000$. Small changes in the mechanical properties of the interfibrillar matrix are thus amplified to apply considerable stress to the elastic fibrils, as a consequence of which the fibrils are more effectively recruited to bear load. Prior biochemical evidence suggests the involvement of proteins like tensilin and NSF in the stiffening of the matrix (31, 38, 39). It is probable that these proteins physically cross-link to the existing glycosaminoglycans and proteoglycans, which in turn are bound to the gap-zones in collagen fibrils. It is conjectured that these proteins are acting like a bridge binding the proteoglycan/GAG sites of two adjacent fibrils together (12, 29). In this manner,

increased matrix stiffening combined with effective shear load transfer to the fibrils enables MCT to undergo considerable (by a factor of ~25; Fig. 6(b)) changes in tissue stiffness. The physical cross-linking process is a time-dependent one (Fig. 1E), most likely due to diffusion of proteins secreted by the JLCs in between the collagen fibrils, combined with progressive occupation of binding sites for these proteins in the interfibrillar matrix. This process of increased interfibrillar stiffening, enabling alteration of mechanical behaviour, is likely to be a general property of MCT in echinoderms.

Conclusion

In summary, in this first direct measurement of the nanoscale fibrillar deformation mechanisms of MCT, we have demonstrated that the mutability of mechanical properties in this unique invertebrate collagenous tissue is achieved solely by interfibrillar matrix cross-linking and un-crosslinking. Increasing interfibrillar cohesion in the mechanically-active state leads to nearly a 50-fold increase in fibrillar stress, underpinning the transition of MCT from a soft- to a stiff-state. A greater fibrillar stress recruitment, mediated by shear transfer from the interfibrillar matrix, leads to an over 20-fold increase in tissue modulus over the timescale of several seconds. The use of *in situ* X-ray methods together with mechanical testing has enabled us to quantify both the material-level mechanisms and the constitutive properties of the components of MCT as they undergo these changes in real time. The ability of MCT to undergo such large changes in stiffness with minimal dimensional changes and solely by increasing fibrillar recruitment highlights the potential of such fibrillar-hydrogel composites to act as dynamic biomaterials that can change their mechanical state rapidly. Such materials could find application as new pharmacological agents, while the design of a new class of mechanically responsive nanocomposites(12) could enable energetically efficient biomaterials and devices that provide not only structural support but can dynamically adjust their properties to the external environment for responding to different demands. The approach opens up several promising further avenues of investigation, e.g. alterations in the molecular level diffraction patterns would provide combined molecular as well as fibrillar real-time structural information, the use of novel synthetic peptides mimicking the stiffening or softening agents in MCT could be tested *in situ* for efficacy(63). Finally the combination of experiments with molecular modelling methods would enable us to link mechanisms at the smallest structural levels to macroscopic behavioural patterns.

Materials and Methods

Dissection of sea cucumber body wall preparations:

Specimens of the sea cucumbers (*Holothuria leucospilota*) were obtained from a commercial wholesaler (Marine Life, Paris, France), and delivered to the synchrotron SAXD beamline (in tanks of artificial sea water) a few hours prior to use. To prepare sea cucumber samples for the mechanical testing in different ionic solutions, we followed a protocol similar that used in previous studies of the mechanics of sea cucumber dermis (19, 64). Specifically, after letting the sea cucumbers rest for 1 hour in sea water, samples from the white central part of the body wall dermis (Fig. 1) were prepared. The attached viscera and muscle layers on the inside were pulled off with forceps, and the pigmented outer dermis was removed using razor blades, leaving only the collagenous part. Rectangular-shaped collagenous tissue pieces (10-20 mm×1.0mm×1.0mm) were cut out using a specialized construct with twin-razor blades fixed on either side of a 1 mm thick steel-section, in order to keep the thickness constant to 1 mm. The sectioning was done in the longitudinal direction of the body wall, used for tensile testing (Fig. 1c-d). While the total length of the sample varied between specimens, the gauge length was kept constant to 6 mm during the tensile testing (as described in the next section). Samples were rinsed in artificial seawater (ASW) after sectioning. After the sections were prepared, and before mechanical testing, all samples were allowed to relax in ASW for 1 hour. Following this, specimens were incubated in ASW (control), high potassium concentration (stiff; high [K⁺]) artificial seawater (KASW), or calcium-free artificial seawater (soft; CaF-ASW) for 1.5 hours. Compositions of these three solutions (ASW, KASW, and CaF-ASW) followed the protocol described previously by Motokawa (14). As expected, this procedure resulted in relative elevation and reduction of stiffness for KASW and CaF-ASW treated dermis, consistent with other studies of chemically treated MCT (30). All studies were carried in accordance with the Animals (Scientific Procedures) Act 1986 of the UK, including revision 2013; invertebrates (except cephalopods) are not considered protected species under the Act.

In situ mechanical testing with SAXD:

A compact micromechanical tester, designed by our group (43), specialized for holding biological tissues and capable of being fixed on the sample stage of a synchrotron SAXD beamline, was used. The tester contains a load cell (100 N rating), with attached amplifier (RDP Electronics Ltd, UK). Strain is applied by displacement of a DC-motor with encoder

(M-126.DG, Physik Instrumente, Karlsruhe, Germany). A customized LabVIEW (National Instruments, UK) interface on a control-PC was used to control the applied tissue strain and strain rates. Adherence of the sample to the tensile tester grips was improved by using sandpaper of various grades between the tissue and the grip. The machine compliance of the tester was measured using a thick steel section. Compliance was found to be negligible compared to the stiffness of the sea cucumber body wall tissue under investigation. Engineering tissue strain (ϵ_{T0}) was calculated from the ratio of the displacement of the sample grips to the unstressed gauge length ~ 6 mm. As MCT is a soft tissue capable of considerable elongation, the engineering tissue strain (ϵ_{T0}) was converted into true tissue strain (ϵ_T) using $\epsilon_T = \ln(1 + \epsilon_{T0})$ (See *Supplementary Information*, section 3)(65). Tissue stress σ was obtained by dividing force by sample area (1.0 mm^2). Rate of increase of stress with tissue strain (tangent modulus E_T (65)) was obtained from a linear regression between σ and ϵ_T with a moving window of $\sim \Delta \epsilon_T = 0.5\%$.

Combined microtensile deformation experiments with time-resolved acquisition of SAXD patterns were carried out at the High Brilliance ID02 beamline at the European Synchrotron Radiation Facility (ESRF, Grenoble, France). Body wall preparations were mounted in the microtensile tester immediately after incubation in test solutions. Samples with gauge length ~ 6 mm were stretched to failure at a constant velocity of 0.01 mm/s (corresponding to a strain rate of $\sim 0.167\%/s$). Samples were kept hydrated by dropwise addition of the incubation solution during the test. SAXD patterns were acquired with a FReLoN CCD detector(66) with a 0.5 second exposure time, using a highly collimated synchrotron X-ray beam (beam size 20 (height) \times 25 (width) μm at sample and detector positions, wavelength $\lambda = 0.9951 \text{ \AA}$ (X-ray energy 12.46 keV) at a sample-to-detector distance of $1006.8 \pm 1.0 \text{ mm}$ determined with silver behenate at the sample position. Each SAXD pattern had a resolution of 2048×2048 pixels and a pixel area of $23.63 \times 23.97 \mu\text{m}^2$. SAXD patterns were collected continuously up to failure of the specimen, with an interval between acquisitions of $\sim 1.5\%$ strain. Each SAXD pattern is therefore acquired on a tissue location which is $\sim 6 \text{ mm} \times 0.015 = 90 \mu\text{m}$ shifted from the previous measurement. The beam diameter is much smaller ($\sim 1/5^{\text{th}}$ of this shift) and there is thus no overlap of the beam onto tissue locations across SAXD measurements. As a result radiation damage, due to multiple exposure of the beam to the same tissue location, is minimized. Radiation damage of protein assemblies and solutions occurs via combination of free radicals produced by water photolysis with free radicals from

the proteins, leading to protein unfolding, aggregation, or breakage (67). Our strategy of continuous sample movement to avoid repeat exposures of the same point is one of several successful approaches to minimize radiation damage (67). Other methods, including continuously replacing the sample (e.g. continuous flow in liquids) or adding radical scavengers to solutions (assuming no structural consequences) (67), are not applicable in the case of strain-stressed tissues considered here. Failure of the specimen usually occurred between 50 and 70% strain. As a result, typically about 40 patterns per sample (60%/1.5% = 40) were acquired.

Determination of fibril strain from SAXD

2D SAXD patterns of sea cucumber body wall collagen were obtained (Fig. 2(b)) and averaged azimuthally (in the angular plane of the X-ray detector) to obtain the Bragg peaks arising from the D-periodicity of SAXD fibrils. The azimuthal average of the intensity provides a 1D intensity profile $I(q)$ (q being the wavevector), which has characteristic Bragg peaks at integer multiples of $2\pi/D$. The software package Fit2D (68) was used, with the CAKE/INTEGRATE command, to carry out the integration. The 5th order peak was used for fitting as it had the strongest peak intensity among the visible Bragg orders, enabling accurate peak fitting and determination of peak shifts (See *Supplementary Information*, section 5). To centre the pattern around the clear 5th order peak at $\sim 0.48 \text{ nm}^{-1}$, inner and outer wavevector limits of 0.45 nm^{-1} and 0.50 nm^{-1} , respectively, were used. Subsequently, the selected 5th order peak was fitted by a Gaussian function with a linear background term to account for the diffuse intensity scattering:

$$I(q) = I_{05} \exp\left(-\frac{1}{2}\left(\frac{q - q_{05}}{w}\right)^2\right) + I_{00} + I'_{01} q \quad \text{Equation 4}$$

Here I_{05} , q_{05} , and w , represent the peak amplitude, peak position and meridional peak width, respectively (I_{00} and I'_{01} are diffuse background terms). The D-period was calculated from the relation $D = 5 \times 2\pi / q_{05}$. The percentage changes in D value at non-zero external force (relative to the unstressed state) provide the critical fibril strain parameter ε_F . The method described here has been used extensively by us for vertebrate collagenous tissues, specifically for bone and tendon (43, 44, 48, 69):

$$\varepsilon_F = \frac{D(\varepsilon_T) - D(\varepsilon_T = 0)}{D(\varepsilon_T = 0)} = \frac{q_0(\varepsilon_T = 0)}{q_0(\varepsilon_T)} - 1 \quad \text{Equation 5}$$

To obtain the fibril strain ratio $\varepsilon_F/\varepsilon_T$ for each sample, a linear regression of fibril strain ε_F versus tissue strain ε_T was carried out (Sigma Plot, Systat Software), and the slope of the linear regression provided $\varepsilon_F/\varepsilon_T$ (43, 46, 48, 50). The values of $\varepsilon_F/\varepsilon_T$ for each sample from the different treatment groups is given in a Table in *Supplementary Information*, section 4.

Determination of fibril orientation measured from SAXD

In a complementary manner to fibril strain, the angular fibril distribution was calculated from the azimuthal intensity profile $I_5(\chi)$ of the 5th order Bragg reflection of the collagen D-spacing. The azimuthal profile was calculated by first integrating (using the Fit2D/CAKE command) the 2D intensity pattern radially in a narrow band of wave-vectors around the peak position $q_{05} \sim 0.48 \text{ nm}^{-1}$ of the 5th order reflection, i.e. over the wavevector range $0.45 - 0.50 \text{ nm}^{-1}$. The background-corrected azimuthal intensity distribution $I_{\text{corrected}}(\chi)$ was calculated by first averaging the azimuthal intensity profiles in two rings around the 5th order peak position, and subtracting the averaged intensity from the centre (peak) ring, as described earlier for bone (70), and is shown in Fig. 2(c1).

$$I_{\text{corrected}}(\chi) = I_{\text{original}}(\chi) - \frac{1}{2}(I_{\text{outer}}(\chi) + I_{\text{inner}}(\chi)) \quad \text{Equation 6}$$

To ensure the full azimuthal width of the peaks was captured, the intensity profile was calculated over the full circle (0 to 360°). Angular coordinates corresponding to high values of $I_{\text{corrected}}(\chi)$ denote a greater proportion of fibrils along the specified azimuthal angle. The profile $I_{\text{corrected}}(\chi)$ was then fitted to a function with two Gaussian peak profiles, separated by 180 degrees.

$$I_{\text{corrected}}(\chi) = I_{0\chi} \left(\exp \left(-\frac{1}{2} \left(\frac{\chi - \chi_0}{\Delta\chi_0} \right)^2 \right) + \exp \left(-\frac{1}{2} \left(\frac{\chi - \chi_0 - \pi}{\Delta\chi_0} \right)^2 \right) \right) \quad \text{Equation 7}$$

The parameter χ_0 defines the main direction of orientation of the fibrils, while $\Delta\chi_0$ is a parameter characterising the width of the distribution and $I_{0\chi}$ is an amplitude term proportional to the total SAXD intensity of the 5th order reflection. It is noted that whilst applied forces will induce shifts in q_{05} over the course of the test, these will turn out (shown in **Results**) to be sufficiently small such that the same narrow band around the initial peak position can be used over the entire test.

A collagen fibril distribution with a narrow angular width (corresponding to well-oriented fibrils) is characterized by a low value $\Delta\chi_0$ and twin sharp peaks in $I_{\text{corrected}}(\chi)$ above a low baseline intensity, while a distribution with a wide angular dispersion in fibril orientation is characterized by high $\Delta\chi_0$ and a nearly constant $I_{\text{corrected}}(\chi)$. We define a dimensionless parameter υ , derived from $I_{\text{corrected}}(\chi)$, which can be used to determine if the fibril distribution is narrow or broad.

$$\upsilon = \text{Std. Dev.}(I_{\text{corrected}}(\chi)) / \text{Mean}(I_{\text{corrected}}(\chi)) \quad \text{Equation 8}$$

It can be seen that an isotropic (wide) fibril angular distribution, corresponding to a nearly constant $I_{\text{corrected}}(\chi)$, will have $\upsilon \sim 0$, while υ will increase as the angular width reduces.

Acknowledgements

The principal SAXD experiments were performed on beamline ID02 at the European Synchrotron Radiation Facility (ESRF), Grenoble, France. JM is supported by the China Scholarship Council (CSC). HSG and MRE acknowledge support from EPSRC (EP/J501360/1), BBSRC (BB/M001644/1) and the Royal Society through the Equipment Grant scheme (SEMF1A6R). LB, HSG and MRE acknowledge support from the Institute of Bioengineering (IoB) at Queen Mary University of London. We thank Jun Ma (School of Engineering and Materials Science, University of London) for help designing the software interface for the tensile tester, Vince Ford (School of Engineering and Materials Science, University of London) for technical support in manufacturing parts for the tensile tester, and T. Narayan (Beamline ID02, ESRF, Grenoble) for excellent support during the beamtime.

Contributions

H. S. Gupta, M. R. Elphick and J. Mo conceived and designed the experiments. J. Mo, S. Prévost and H. S. Gupta performed the *in-situ* SAXD experiments. J. Mo performed the Trichrome staining experiment with L. M. Blowes and M. Egertová. J. Mo and H. S. Gupta performed the modelling calculations. J. Mo prepared the figures. J. Mo and H. S. Gupta analysed the data and wrote the manuscript. H. S. Gupta and W. Wang supervised the project. All the authors participated in discussion of results and revised the manuscript.

References

1. Egan P, Sinko R, LeDuc PR, & Keten S (2015) The role of mechanics in biological and bio-inspired systems. *Nat Commun* 6:1–12.

- 575 2. Meyers MA, Chen PY, Lin AYM, & Seki Y (2008) Biological materials: Structure
576 and mechanical properties. *Prog Mater Sci* 53(1):1-206.
- 577 3. Fung Y-c (2013) *Biomechanics: mechanical properties of living tissues* (Springer
578 Science & Business Media).
- 579 4. Weinkamer R DJ, Brechet Y, & Fratzl P (2013) All but diamonds-Biological
580 materials are not forever. *Acta Mater* 61(3):880-889.
- 581 5. Eyre DR (1980) Collagen: Molecular Diversity in the Body's Protein Scaffold.
582 *Science* 207(4437):1315-1322.
- 583 6. Harrington MJ, Masic A, Holten-Andersen N, Waite JH, & Fratzl P (2010) Iron-Clad
584 Fibers: A Metal-Based Biological Strategy for Hard Flexible Coatings. *Science*
585 328(5975):216-220.
- 586 7. Fratzl P, Fratzlzelman N, & Klaushofer K (1993) Collagen Packing And
587 Mineralization - an X-Ray-Scattering Investigation Of Turkey Leg Tendon. *Biophys J*
588 64(1):260-266.
- 589 8. Ciarletta P & Amar MB (2009) A finite dissipative theory of temporary interfibrillar
590 bridges in the extracellular matrix of ligaments and tendons. *J R Soc Interface* 6(39):909-924.
- 591 9. Julicher F, Ajdari A, & Prost J (1997) Modeling molecular motors. *Rev Mod Phys*
592 69(4):1269-1281.
- 593 10. Motokawa T (1984) Connective-Tissue Catch In Echinoderms. *Biol Rev* 59(2):255-
594 270.
- 595 11. Wilkie IC (1984) Variable Tensility In Echinoderm Collagenous Tissues - a Review.
596 *Mar Behav Physiol* 11(1):1-34.
- 597 12. Wilkie I (2005) Mutable collagenous tissue: overview and biotechnological
598 perspective. *Echinodermata*, (Springer), pp 221-250.
- 599 13. Motokawa T (1994) Effects of ionic environment on viscosity of Triton-extracted
600 catch connective tissue of a sea cucumber body wall. *Comparative Biochemistry and*
601 *Physiology Part B: Comparative Biochemistry* 109(4):613-622.
- 602 14. Motokawa T & Tsuchi A (2003) Dynamic mechanical properties of body-wall dermis
603 in various mechanical states and their implications for the behavior of sea cucumbers. *Biol*
604 *Bull-Us* 205(3):261-275.
- 605 15. Ribeiro AR, *et al.* (2011) New insights into mutable collagenous tissue: correlations
606 between the microstructure and mechanical state of a sea-urchin ligament. *PLoS one*
607 6(9):e24822.
- 608 16. Di Benedetto C, *et al.* (2014) Production, Characterization and Biocompatibility of
609 Marine Collagen Matrices from an Alternative and Sustainable Source: The Sea Urchin
610 *Paracentrotus lividus*. *Mar Drugs* 12(9):4912-4933.
- 611 17. Wilkie IC, *et al.* (2015) Mechanical Properties of the Compass Depressors of the Sea-
612 Urchin *Paracentrotus lividus* (Echinodermata, Echinoidea) and the Effects of Enzymes,
613 Neurotransmitters and Synthetic Tensilin-Like Protein. *Plos One* 10(3).
- 614 18. Birenheide R & Motokawa T (1996) Contractile connective tissue in crinoids. *Biol*
615 *Bull-Us* 191(1):1-4.
- 616 19. Takemae N, Nakaya F, & Motokawa T (2009) Low Oxygen Consumption and High
617 Body Content of Catch Connective Tissue Contribute to Low Metabolic Rate of Sea
618 Cucumbers. *Biol Bull-Us* 216(1):45-54.
- 619 20. Barbaglio A, *et al.* (2012) The mechanically adaptive connective tissue of
620 echinoderms: its potential for bio-innovation in applied technology and ecology. *Marine*
621 *environmental research* 76:108-113.
- 622 21. Jordan H (1914) Die Holothurien als hohlorganartige Tiere und die Tonusfunktion
623 ihrer Muskulatur. *Zool. Jahrb. Abt.* 34:365-436.

22. Motokawa T (1981) The stiffness change of the holothurian dermis caused by chemical and electrical stimulation. *Comparative Biochemistry and Physiology Part C: Comparative Pharmacology* 70(1):41-48.
23. Motokawa T (1982) Factors regulating the mechanical properties of holothurian dermis. *Journal of Experimental Biology* 99:29-41.
24. Wilkie IC, Carnevali MDC, & Bonasoro F (1992) The Compass Depressors Of Paracentrotus-Lividus (Echinodermata, Echinoida) - Ultrastructural And Mechanical Aspects Of Their Variable Tensility And Contractility. *Zoomorphology* 112(3):143-153.
25. M H & K T (1983) Fine structure and mechanical properties of the catch apparatus of the sea-urchin spine, a collagenous connective tissue with muscle-like holding capacity. *Journal of Experimental Biology* 103(1):1-14.
26. Diab M & Gilly WF (1984) Mechanical properties and control of non-muscular catch in spine ligaments of the sea urchin, Strongelocentrotus franciscanus. *Journal of Experimental Biology* 111(1):155-170.
27. Szulgit G & Shadwick R (1994) The effects of calcium chelation and cell perforation on the mechanical properties of sea urchin ligaments. *Echinoderms through time*:887-892.
28. Trotter JA & Koob TJ (1989) Collagen and proteoglycan in a sea urchin ligament with mutable mechanical properties. *Cell Tissue Res* 258(3):527-539.
29. Trotter JA, LyonsLevy G, Thurmond FA, & Koob TJ (1995) Covalent composition of collagen fibrils from the dermis of the sea cucumber, Cucumaria frondosa, a tissue with mutable mechanical properties. *Comp Biochem Phys A* 112(3-4):463-478.
30. Motokawa T (2011) Mechanical mutability in connective tissue of starfish body wall. *The Biological Bulletin* 221(3):280-289.
31. Yamada A, Tamori M, Iketani T, Oiwa K, & Motokawa T (2010) A novel stiffening factor inducing the stiffest state of holothurian catch connective tissue. *The Journal of experimental biology* 213(20):3416-3422.
32. Oji T & Okamoto T (1994) Arm autotomy and arm branching pattern as anti-predatory adaptations in stalked and stalkless crinoids. *Paleobiology* 20(1):27-39.
33. Trotter JA, Chapman JA, Kadler KE, & Holmes DF (1998) Growth of sea cucumber collagen fibrils occurs at the tips and centers in a coordinated manner. *J Mol Biol* 284(5):1417-1424.
34. Trotter JA, *et al.* (1996) Stiparin: a glycoprotein from sea cucumber dermis that aggregates collagen fibrils. *Matrix biology* 15(2):99-110.
35. Koob TJ, Koob-Emunds MM, & Trotter JA (1999) Cell-derived stiffening and plasticizing factors in sea cucumber (Cucumaria frondosa) dermis. *Journal of experimental biology* 202(17):2291-2301.
36. Cluzel C, Lethias C, Humbert F, Garrone R, & Exposito JY (2001) Characterization of fibrosurfin, an interfibrillar component of sea urchin catch connective tissues. *J Biol Chem* 276(21):18108-18114.
37. Motokawa T (1982) Factors Regulating the Mechanical-Properties of Holothurian Dermis. *Journal of Experimental Biology* 99(Aug):29-41.
38. Koob TJ, Koob-Emunds MM, & Trotter JA (1999) Cell-derived stiffening and plasticizing factors in sea cucumber (Cucumaris frondosa) dermis. *Journal Of Experimental Biology* 202(17):2291-2301.
39. Tipper JP, Lyons-Levy G, Atkinson MA, & Trotter JA (2002) Purification, characterization and cloning of tensilin, the collagen-fibril binding and tissue-stiffening factor from Cucumaria frondosa dermis. *Matrix biology* 21(8):625-635.
40. Trotter JA, *et al.* (1999) Collagen fibril aggregation-inhibitor from sea cucumber dermis. *Matrix Biology* 18(6):569-578.

41. Ribeiro AR, *et al.* (2012) Matrix Metalloproteinases in a Sea Urchin Ligament with Adaptable Mechanical Properties. *Plos One* 7(11).
42. Cluzel C, Lethias C, Garrone R, & Exposito JY (2004) Distinct Maturation of N-propeptide Domains in Fibrillar Procollagen Molecules Involved in the Formation of Heterotypic Fibrils in Adult Sea Urchin Collagenous Tissues. *J Biol Chem* 279:9811-9817.
43. Gupta HS, *et al.* (2013) Intrafibrillar plasticity through mineral/collagen sliding is the dominant mechanism for the extreme toughness of antler bone. *J Mech Behav Biomed* 28:366-382.
44. Screen H, Seto J, Krauss S, Boesecke P, & Gupta H (2011) Extrafibrillar diffusion and intrafibrillar swelling at the nanoscale are associated with stress relaxation in the soft collagenous matrix tissue of tendons. *Soft Matter* 7(23):11243-11251.
45. Zimmermann EA, *et al.* (2013) Mechanical adaptability of the Bouligand-type structure in natural dermal armour. *Nat Commun* 4.
46. Zimmermann EA, *et al.* (2011) Age-related changes in the plasticity and toughness of human cortical bone at multiple length scales. *Proceedings of the National Academy of Sciences of the United States of America* 108(35):14416-14421.
47. Hulmes D, Jesior J-C, Miller A, Berthet-Colominas C, & Wolff C (1981) Electron microscopy shows periodic structure in collagen fibril cross sections. *Proceedings of the National Academy of Sciences* 78(6):3567-3571.
48. Gupta HS, *et al.* (2006) Cooperative deformation of mineral and collagen in bone at the nanoscale. *Proceedings of the National Academy of Sciences* 103(47):17741-17746.
49. Stock SR & Almer JD (2009) Strains in bone and tooth via high energy X-ray scattering. *Bone* 44(2):S270-S270.
50. Puxkandl R, *et al.* (2002) Viscoelastic properties of collagen: synchrotron radiation investigations and structural model. *Philosophical Transactions of the Royal Society of London B: Biological Sciences* 357(1418):191-197.
51. Gasser TC, *et al.* (2012) Spatial orientation of collagen fibers in the abdominal aortic aneurysm's wall and its relation to wall mechanics. *Acta Biomater* 8(8):3091-3103.
52. Linari M, *et al.* (2015) Force generation by skeletal muscle is controlled by mechanosensing in myosin filaments. *Nature* 528(7581):276-279.
53. Yang W, *et al.* (2015) On the tear resistance of skin. *Nat Commun* 6.
54. Capadona JR, Shanmuganathan K, Tyler DJ, Rowan SJ, & Weder C (2008) Stimuli-responsive polymer nanocomposites inspired by the sea cucumber dermis. *Science* 319(5868):1370-1374.
55. Eppell SJ, Smith BN, Kahn H, & Ballarini R (2006) Nano measurements with micro-devices: mechanical properties of hydrated collagen fibrils. *J R Soc Interface* 3(6):117-121.
56. Fratzl P (2008) *Collagen: structure and mechanics, an introduction* (Springer US).
57. Jager I & Fratzl P (2000) Mineralized collagen fibrils: A mechanical model with a staggered arrangement of mineral particles. *Biophys J* 79(4):1737-1746.
58. Gao HJ, Ji BH, Jager IL, Arzt E, & Fratzl P (2003) Materials become insensitive to flaws at nanoscale: Lessons from nature. *Proceedings of the National Academy of Sciences of the United States of America* 100(10):5597-5600.
59. Fratzl P (2007) Nature's hierarchical materials. *Nature's hierarchical materials* 52(8):1263-1334.
60. Trotter JA, Thurmond FA, & Koob TJ (1994) Molecular-Structure and Functional-Morphology of Echinoderm Collagen Fibrils. *Cell Tissue Res* 275(3):451-458.
61. Masic A, *et al.* (2015) Osmotic pressure induced tensile forces in tendon collagen. *Nat Commun* 6:5942.

62. Scott JE (1990) Proteoglycan: collagen interactions and subfibrillar structure in collagen fibrils. Implications in the development and ageing of connective tissues. *J Anat* 169:23-35.
63. Elphick MR (2012) The protein precursors of peptides that affect the mechanics of connective tissue and/or muscle in the echinoderm *Apostichopus japonicus*. *Plos One* 7(8).
64. Tamori M, et al. (2006) Tensilin-like stiffening protein from *Holothuria leucospilota* does not induce the stiffest state of catch connective tissue. *Journal of Experimental Biology* 209(9):1594-1602.
65. Vincent JF (2012) *Structural biomaterials* (Princeton University Press).
66. Narayanan T, Diat O, & Boesecke P (2001) SAXS and USAXS on the high brilliance beamline at the ESRF. *Nuclear Instruments and Methods in Physics Research Section A: Accelerators, Spectrometers, Detectors and Associated Equipment* 467:1005-1009.
67. Jeffries CM, Graewert MA, Svergun DI, & Blanchet CE (2015) Limiting radiation damage for high-brilliance biological solution scattering: practical experience at the EMBL P12 beamline PETRAIII. *J Synchrotron Radiat* 22:273-279.
68. Hammersley A (1997) FIT2D: an introduction and overview. *European Synchrotron Radiation Facility Internal Report* 68.
69. Karunaratne A, et al. (2012) Significant deterioration in nanomechanical quality occurs through incomplete extrafibrillar mineralization in rachitic bone: evidence from in-situ synchrotron X-ray scattering and backscattered electron imaging. *Journal of bone and mineral research : the official journal of the American Society for Bone and Mineral Research* 27(4):876-890.
70. Karunaratne A, et al. (2016) Multiscale alterations in bone matrix quality increased fragility in steroid induced osteoporosis. *Bone* 84:15-24.

747 Figures and Figure Legends

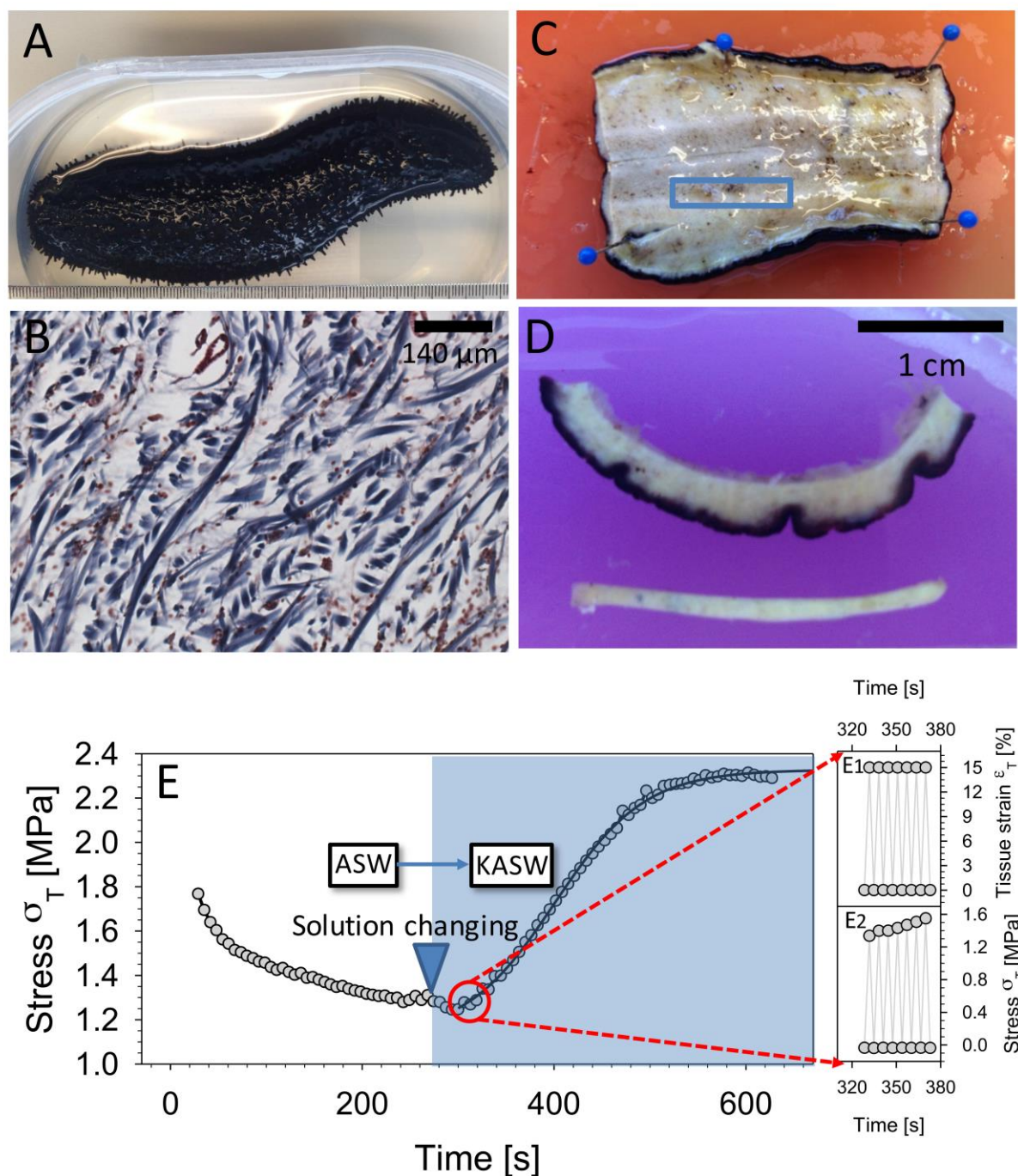


Figure 1: Sea cucumber body wall mutable collagenous tissue (MCT). (a) Sea cucumber *Holothuria leucospilota* (b) Transverse section of sea cucumber body wall stained using Masson's Trichrome method; collagen fibrils appear blue (c) The sheet of body wall after animal was cut in half along the longitudinal plane. The blue rectangle indicates the dimensions and location of sectioned specimen, with the long dimension along the longitudinal axis. (d) View of sectioned sea cucumber dermis including dark outer dermis and

inner layer, below is the tensile test specimen. Prior to testing, the dark-pigmented outer dermis as well as the inner layer was removed, leaving only the centre part of the specimen. (e) Time-dependent change in sea cucumber MCT mechanics induced via ionic treatment. The peak stress (per cycle) is plotted during strain-controlled cyclic loading of sea cucumber dermis at 0.3 Hz (to 15% tissue strain), with tissue immersed in ASW until ~290 s, followed by a change of the immersing solution to KASW (stiffening agent). A clear rise of peak stress (per cycle) is observed, fitted with a sigmoidal curve as a guide to the eye. Inset figures on the right show a magnified time-range over a few (seven) cycles, with both maximum and minimum stress and strain indicated.

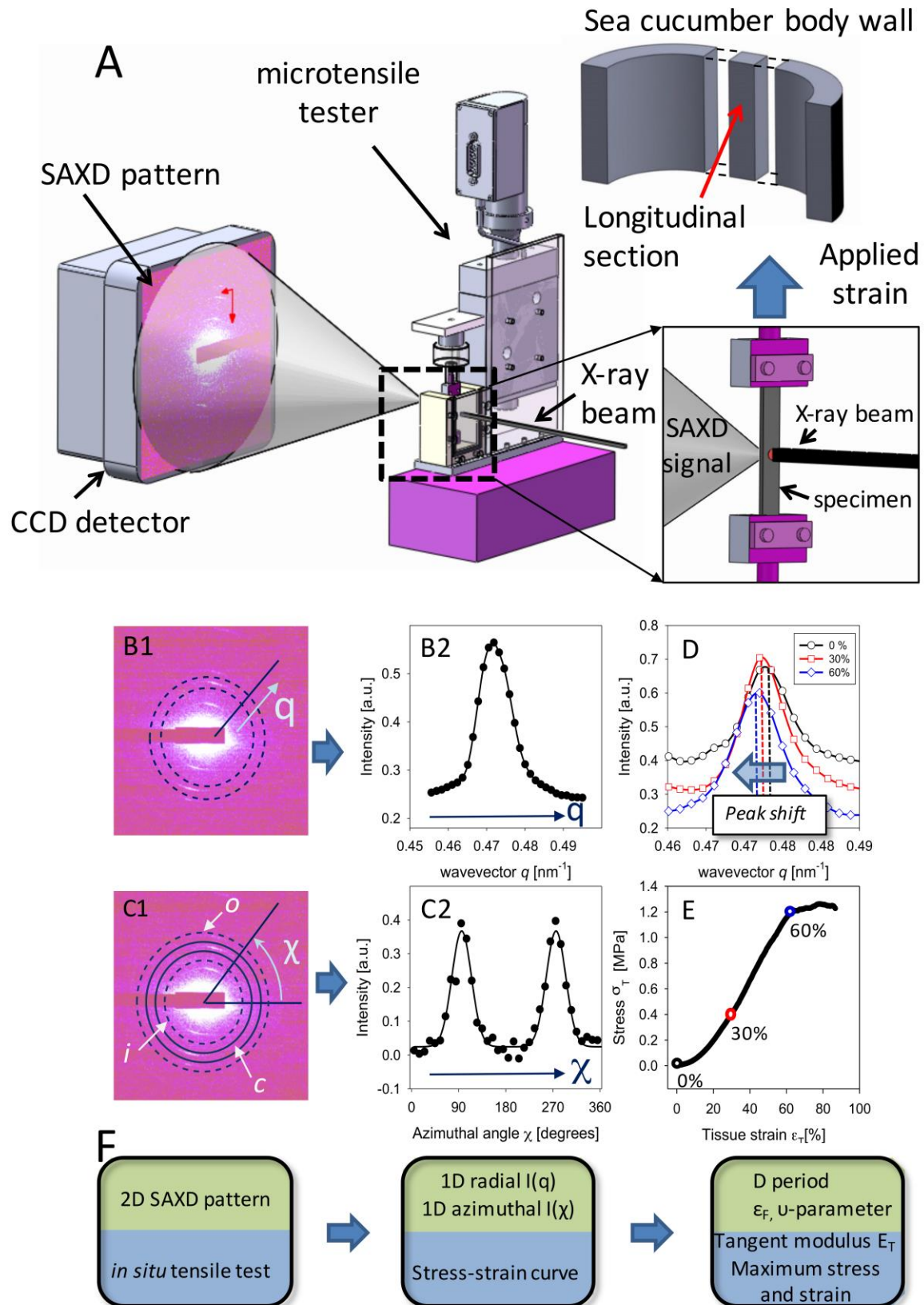


Figure 2: In situ nanomechanics with synchrotron small angle X-ray diffraction (SAXD): (a) *Experimental configuration:* Tensile tester (centre) with MCT specimen mounted along X-ray beam path in transmission geometry with CCD detector (left). Right

Link to PNAS website (open access): <http://www.pnas.org/cgi/doi/10.1073/pnas.1609341113>

inset: magnified view of sample in chamber, and incident X-ray beam (right) with SAXD scattering shown on left. The tensile strain is applied along the vertical direction. Upper right: Schematic of body wall of sea cucumber shown in **Figure 1**, with tensile test specimen sectioned with long axis parallel to the long axis of the animal. *Data reduction pipeline*: (b1) a two-dimensional SAXD pattern from collagen fibrils in sea cucumber dermis MCT with predominant fibril orientation vertical; radial (q) direction indicated. Dotted lines denote the ring over which the azimuthal averaging of intensity is carried out. (b2) The azimuthally averaged radial intensity profile $I(q)$ for the pattern in (b1). (c1) The same 2D SAXD pattern as (b1), with the inner, outer and central rings (i , o and c respectively on the figure) shown schematically, over which radial averaging of intensity is carried out; azimuthal (χ) direction indicated. (c2) The radially averaged intensity profile $I(\chi)$. In (b2) and (c2) both experimental data (open circles) and fits to model functions (solid lines) are shown. (d) Radial intensity profile $I(q)$ for three levels of applied tissue strain $\varepsilon_T = 0\%$ (circles), 30% (squares) and 60% (diamonds), showing the shift of peak position to lower wavevector with increasing strain. (e) Tissue stress-tissue strain plot for sea cucumber dermis in tension, with circles (black: 0%; red: 30%; blue: 60% (colour online)) indicating the points from which the $I(q)$ plots in (d) are shown. (f) Flowchart corresponding to the data reduction steps in (b1-c2) above, with parameters obtained at each step indicated.

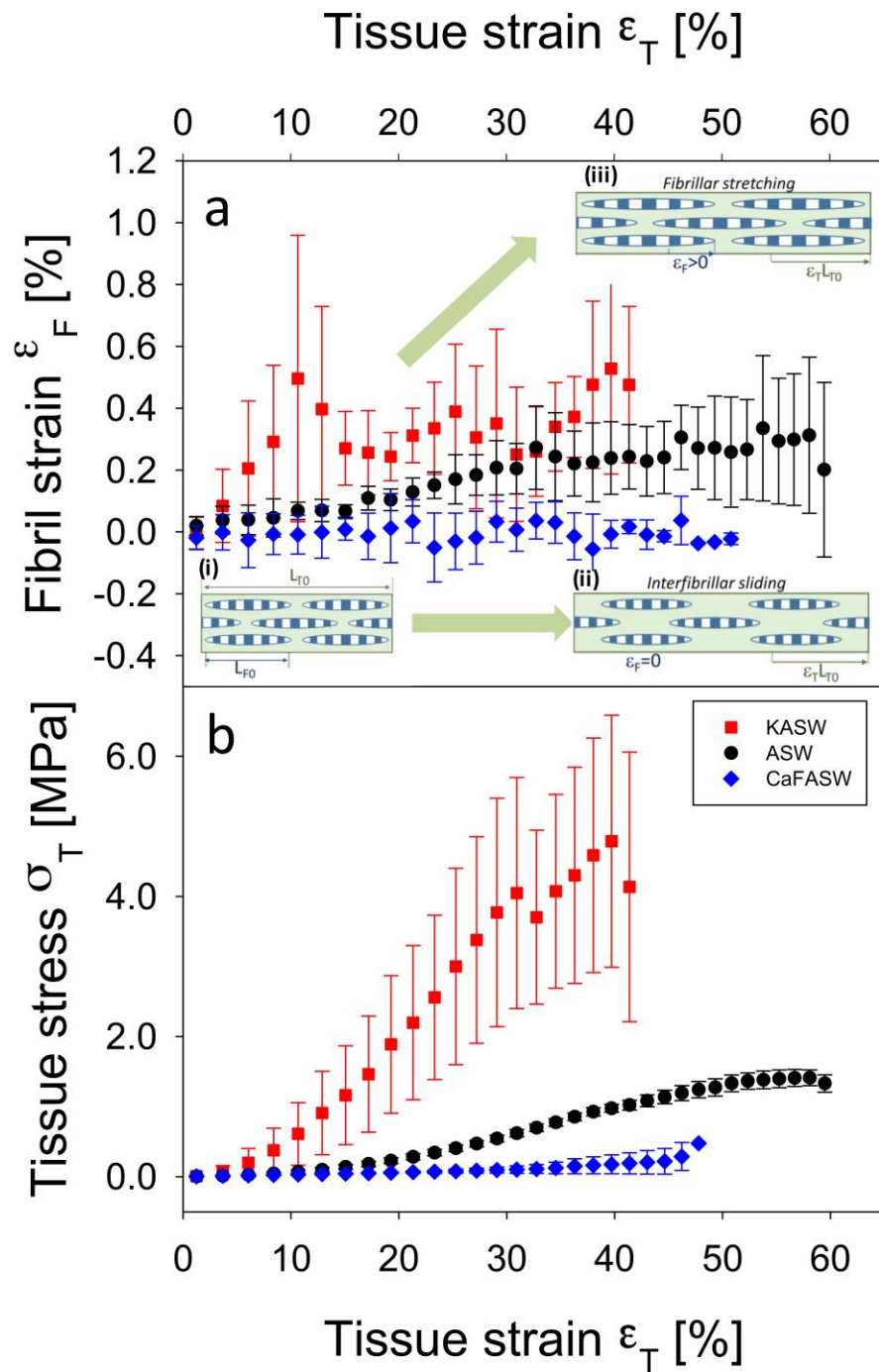


Figure 3: Altered fibrillar stress- and strain take-up in ionically-treated MCT. (a) Fibril strain versus applied tissue strain from ionically treated sections of MCT dermis, measured from the peak shifts of the 5th order collagen reflections in the SAXD pattern. The rate of increase of fibril strain with tissue strain ($\varepsilon_F/\varepsilon_T$) is proportional to the amount of stress taken

up by the collagen fibrils. Data from control (ASW): black circles, $n=4$; stiffened (KASW): red squares, $n=4$; and softened (CaF-ASW): blue diamonds, $n=3$. All samples in each group are binned according to tissue strain with bin widths of 2.0%; error bars are standard deviations. Stiffened MCT exhibits a higher rate of increase of fibril strain compared to control, whilst softened MCT shows essentially no increase in fibril strain. Inset schematics (i) Fibrils (striated ellipsoids; length L_{F0}) separated by interfibrillar matrix, in unloaded MCT of length L_{T0} . (ii) In softened MCT (CaF-ASW treated), while the tissue elongates ($\epsilon_T > 0$), the fibrils do not stretch, but slide in the interfibrillar matrix ($\epsilon_F = 0$). (iii) In stiffened MCT (KASW treated), there is increased stress transfer to the fibrils, leading to fibrillar stretching ($\epsilon_F > 0$). (b) Corresponding macroscopic tensile stress/strain curves for the control, stiffened and softened groups, binned according to tissue strain (error bars: standard deviations), showing clear differences in tangent modulus and maximum stress achieved.

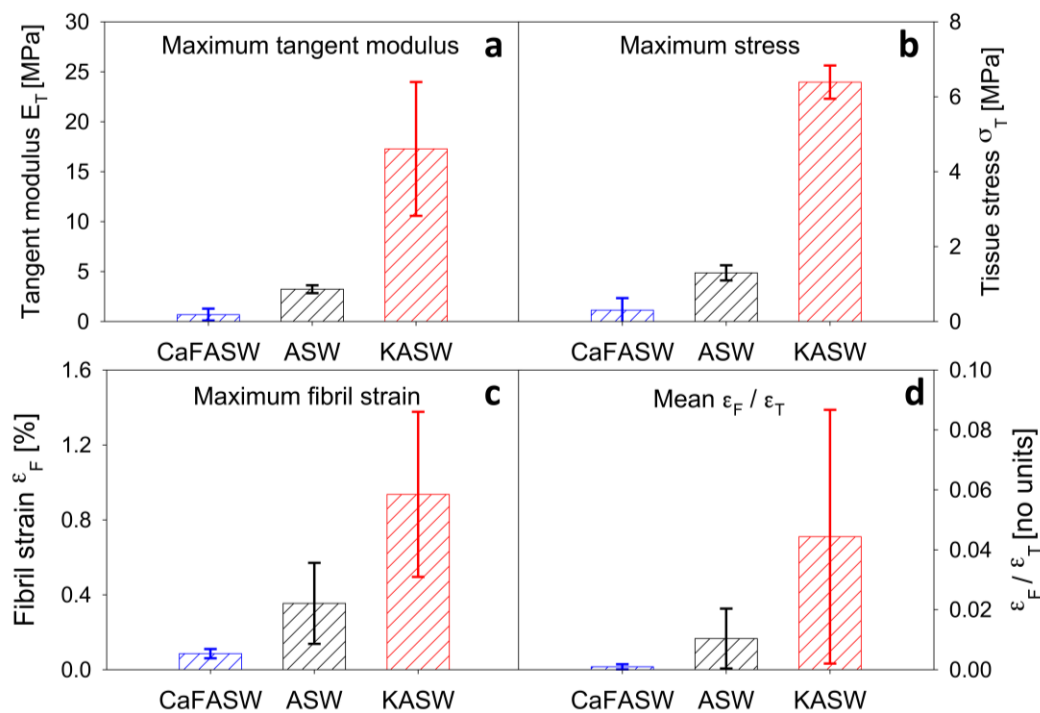


Figure 4: Quantified MCT mechanics. (a) Averaged maximum tangent modulus and (b) maximum stress for control (ASW; black; $n=4$), stiffened (KASW; red; $n=4$) and softened (CaF-ASW; blue; $n=3$) specimens from MCT dermis; error bars are standard deviations. n denotes the number of samples in each treatment group. At the tissue level, stiffened MCT always exhibits remarkably higher mechanical properties compared to the control group, and for the softened one, the binned maximum tangent modulus and the maximum stress is almost negligible. At the fibrillar level, the fibril strain (c) and the ratio of the fibril strain to

Link to PNAS website (open access): <http://www.pnas.org/cgi/doi/10.1073/pnas.1609341113>

tissue strain ((d); the fraction of the deformation taken up at the fibril level) for the stiffened, control and softened MCT follows the same trend with properties at the tissue level.

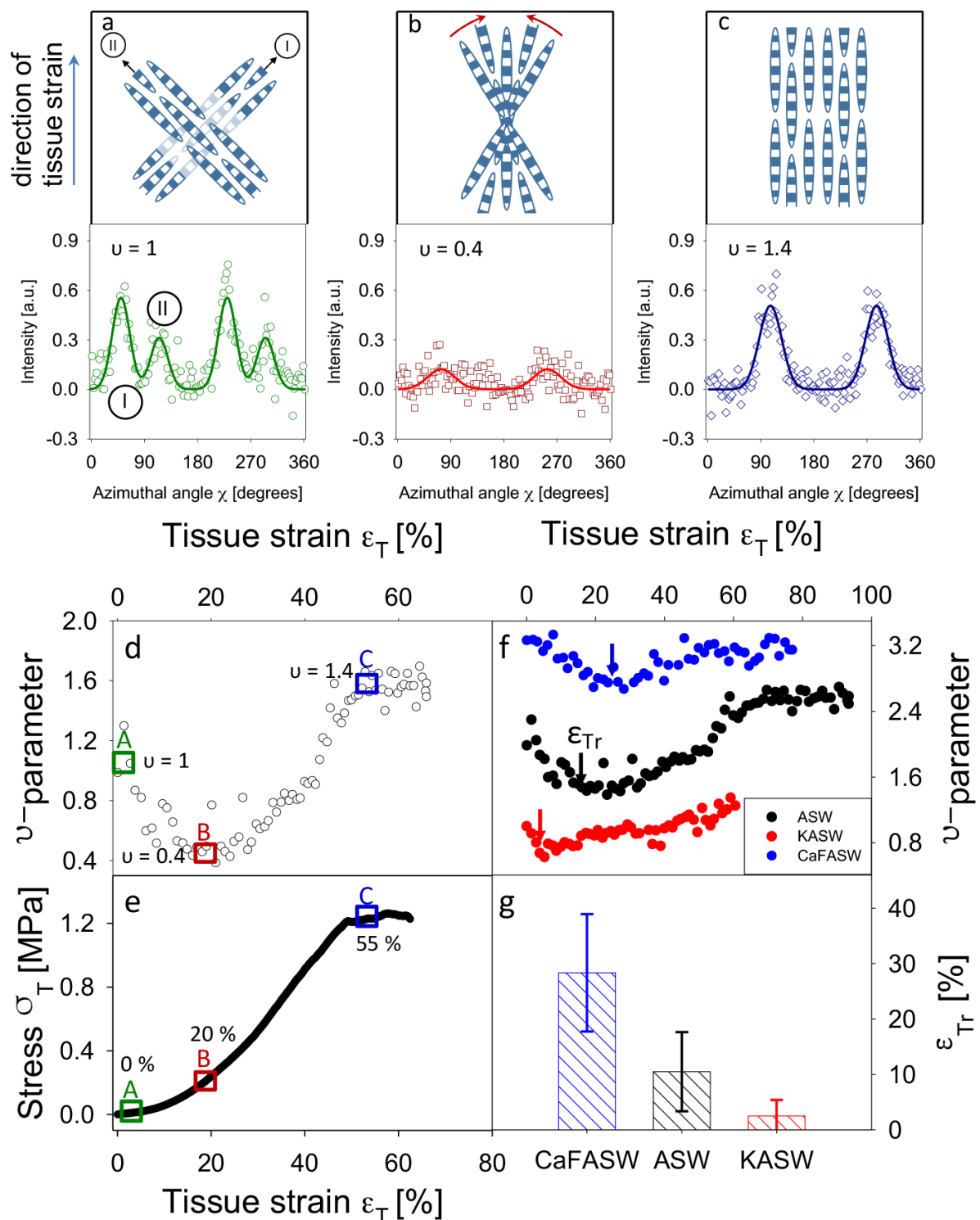


Figure 5: Strain-induced fibril alignment of MCT in stiffened, control and softened states: (a)-(c) Top row: schematic illustration of fibril distribution at increasing tissue strain levels; Bottom row: corresponding $I(\chi)$ plots for a control (ASW) sample with corresponding ν -parameter. The vertical arrow to the left of the plots indicates the direction of applied tissue strain. Link to PNAS website (open access): <http://www.pnas.org/cgi/doi/10.1073/pnas.1609341113>

strain. (a) (0% strain) shows bimodal distribution due to two groups of fibres (I and II) inclined to the direction of tensile load at two principal fibre directions (arrows). In the $I(\chi)$ profile below, the two sets of peaks arising from these two groups of fibres are labelled I and II, respectively. (b) (20% strain) shows a wider range of orientations due to fibrils progressively reorienting (indicated by the red arcing arrows) toward the tensile axis (low ν) and (c) (55% strain) shows highly aligned fibres along the vertical direction (higher ν) (d) Initial decrease followed by increase of ν -parameter with increase tissue strain, for control (ASW) MCT, exhibiting an initial decrease, a local minimum at tissue strain $\sim 20\%$, followed by an increase. (e) A typical stress-strain curve for ASW-treated MCT. In (d) and (e), rectangles indicate strain locations corresponding to (a)-(c). (f) Variation of the strain-induced changes in the ν -parameter as a function of the mechanical state of MCT due to ionic treatment. Data from one representative MCT specimen in each state is shown. The tissue strain corresponding to the local minimum in ν is indicated by a vertical arrow, denoted ϵ_{Tr} , and is lowest for the stiffened and highest for the softened specimen. (g) Averaged ϵ_{Tr} across the three treatments (control (ASW; black; $n=4$), stiffened (KASW; red; $n=4$) and softened (CaF-ASW; blue; $n=3$)); error bars are standard deviations.

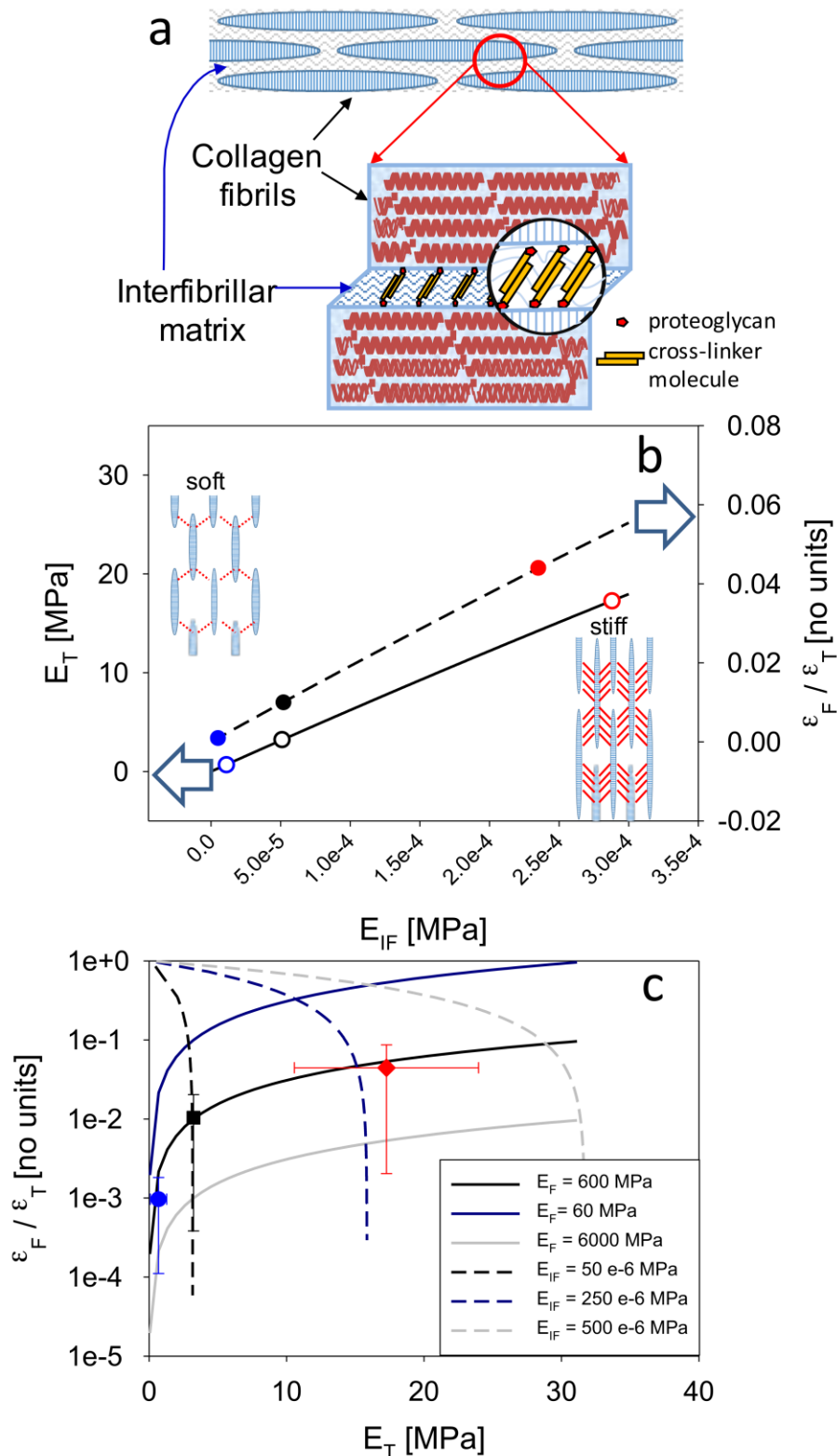


Figure 6: Staggered model of MCT nanomechanics. (a) Staggered model for MCT: discontinuous, spindle-shaped collagen fibrils aggregating in parallel. The attached PGs serve as a binding site for inter-fibrillar cohesion mediated by cross-linker molecules (12). (b) Elevation of inter-fibrillar stiffness E_{IF} leads to a corresponding increase in both tissue stiffness E_T and the normalized strain ratio ϵ_F / ϵ_T . (c) Plot of the normalized strain ratio ϵ_F / ϵ_T versus tissue stiffness E_T for various values of E_F and E_{IF} . Link to PNAS website (open access): <http://www.pnas.org/cgi/doi/10.1073/pnas.1609341113>

modulus E_T (left hand abscissa; solid line: staggered model prediction) and fibril-to-tissue strain ratio (ϵ_F/ϵ_T) (right hand abscissa; dashed line: staggered model prediction). Symbols show experimental values for each tissue group with E_{IF} calculated from the staggered model equations (filled symbols: from **Equation** (1); open symbols: from **Equation** (2)). Open arrows indicate the abscissa each line belongs to. The inset schematics show the shear transfer, and consequent stress take-up, between fibrils in softened (left) and stiffened (right) states. Increased shear stress in the stiffened interfibrillar matrix is shown qualitatively by a larger number of interfibrillar shear lines. (c) Positive correlation between ϵ_F/ϵ_T and E_T demonstrates that interfibrillar stiffening is the mechanism for alteration of MCT mechanics. The staggered-model relations between (ϵ_F/ϵ_T) and E_T (**Equation** 3) are shown via solid curves (with a positive gradient) for varying E_{IF} and three fixed levels of E_F (blue: 60 MPa, black: 600 MPa, and grey: 6000 MPa). Likewise, dashed lines show staggered-model predictions for (ϵ_F/ϵ_T) vs. E_T for varying E_F and three fixed levels of E_{IF} (black: 50×10^{-6} MPa, dark blue: 250×10^{-6} MPa, and grey: 500×10^{-6} MPa). Symbols show experimental (ϵ_F/ϵ_T) and E_T , which show a clear positive correlation, indicating interfibrillar stiffening (blue: CaF-ASW, black: ASW and red: KASW; error bars are standard deviations).

